Earth, Planets and Space

EXPRESS LETTER

Open Access

Fine structure of a daytime mid-latitude sporadic-E revealed by GNSS TEC, InSAR, and MAI

Tatsuya Fujimoto[1], Masato Furuya[2*] and Kosuke Heki[3]

Abstract

Combining the total electron content (TEC) data from two nationwide Global Navigation Satellite System (GNSS) networks in Japan with the *L*-band synthetic aperture radar (SAR) data, we reveal the fine spatial and temporal structure of a daytime sporadic-*E* (Es) episode in Shikoku, Japan. The snapshot of the Es is derived not only from interferometric SAR (InSAR) but also from multiple aperture interferometry (MAI), the latter of which performs better in isolating the fine spatial structure. The GNSS TEC maps indicate that the Es episode is accompanied by a primary east–west elongated (up to ~ 180 km) southward migrating TEC striation with a speed of ~ 90 m/s and ~ 10–20 km widths in the north–south direction. As previously suggested by the GNSS TEC time series, the present InSAR and MAI data independently confirm that electron density in the primary striation gradually increases from the frontal leading edge but abruptly drops in the trailing edge. MAI-based TEC map confirms multiple TEC striations as previously suggested in GNSS TEC time-series, which are reminiscent of the quasi-periodic (QP) echoes in nighttime Es detected by the middle and upper atmosphere (MU) radar, but the periodicity is not as clear as that observed by MU radar. The Kelvin–Helmholtz (KH) instabilities around the wind shear of neutral winds could be responsible for the QP TEC striations.

Keywords Ionosphere, Sporadic-E, GNSS-TEC, ALOS-2, PALSAR-2, InSAR, MAI

*Correspondence:
Masato Furuya
furuya@sci.hokudai.ac.jp
Full list of author information is available at the end of the article

Graphical abstract

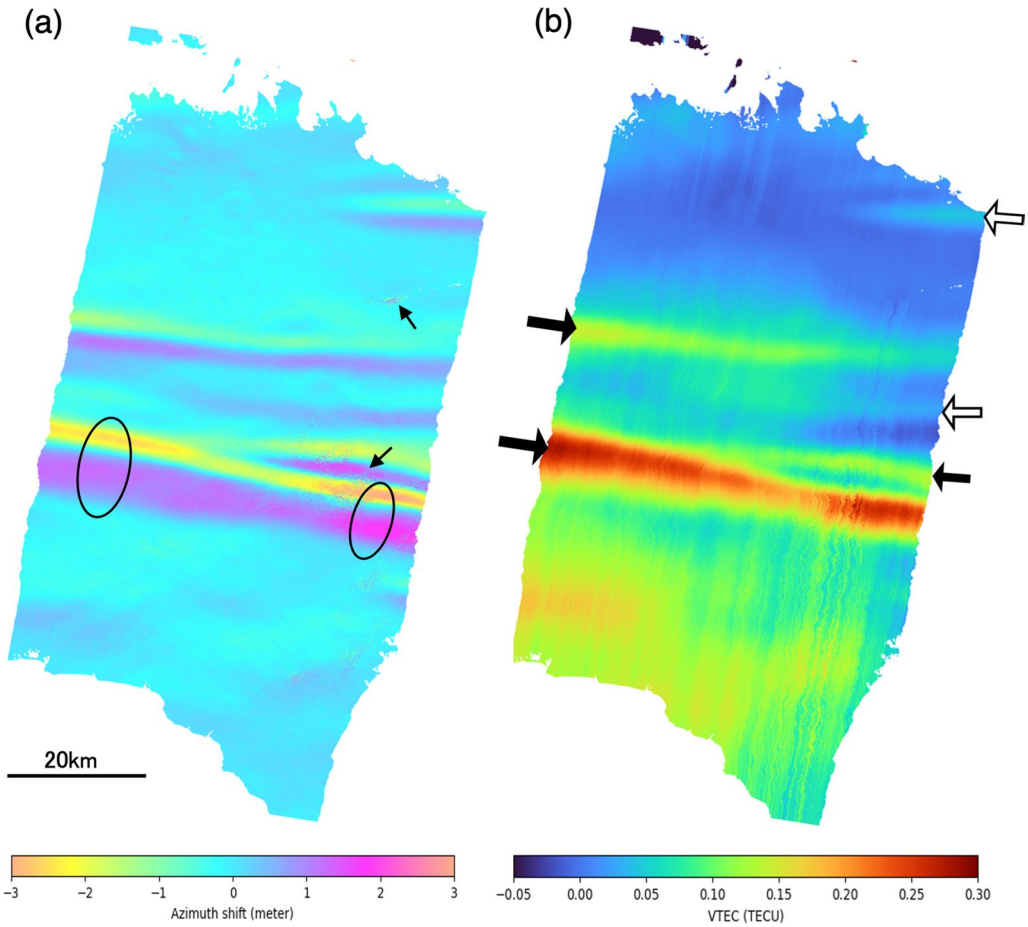

1 Introduction

Sporadic-*E* (Es) layer is an anomalously high electron density patch that appears at altitudes of ~ 100 km in the E region of the ionosphere, causing communication problems in the very high frequency (VHF) band and has been studied for decades to understand its spatial and temporal characteristics and generation mechanisms (e.g., Whitehead 1989; Mathews 1998; Haldoupis 2011). Conventional pointwise measurements by ionosonde and ground-based radars, including the Middle and Upper atmosphere (MU) radar (e.g., Yamamoto et al. 1991), have a generally good temporal resolution but are sparsely distributed and thus the detailed spatial structure and temporal evolution of Es are uncertain. Over the last decade, spatially dense Global Navigation Satellite System (GNSS) receivers' network allowed to reveal the details of daytime Es events with the use of GNSS Total Electron Content (TEC), the number of free electrons integrated along the line of sight (LOS) from GNSS satellites to receivers (e.g., Maeda and Heki 2014, 2015; Muafiry et al. 2018; Sun et al. 2021). Moreover, while only the US Global Positioning System satellites were used in earlier studies (e.g., Maeda and Heki 2014, 2015; Sun et al. 2021), multi-GNSS satellites, including Russian GLONASS, European Union's Galileo, Japanese Quasi-Zenith Satellite System (QZSS), and Chinese Beidou system, are now available and can improve the spatial resolution and coverage (Muafiry et al. 2018). Furthermore, another dense GNSS continuous observation network by SoftBank Corporation, a private cell phone company, became available in Japan with ~ 3300 receivers for real-time kinematic GNSS service. Ohta and Ohzono (2022) demonstrated that the data quality of the SoftBank network was comparable to the Japanese GNSS Earth Observation Network (GEONET) data for geodetic studies, indicating the capability to increase the GNSS receivers' density

further. With the combination of the GEONET and SoftBank networks, the spatial separation of the ground GNSS receivers can reach 1 km or better, depending on the area.

Satellite-based L-band interferometric synthetic aperture radar (InSAR) complements the coarse distribution of GNSS receivers on the ground because of much higher spatial resolution than 100 m with wide area coverage; because one InSAR image is generated from two SAR images called primary and secondary ones (e.g., Hanssen 2001; Simons and Rosen 2015), the temporal resolution is limited by the recurrent period of the satellite on the order of 10 days, depending on the design of orbit and the availability of satellite. Although the chances to detect Es by InSAR are further limited because the Es event must take place during the instant of SAR imaging, Maeda et al. (2016) first succeeded in imaging an Es event using the *L*-band Advanced Land Observation Satellite (ALOS) Phased Array-type Synthetic Aperture Radar (PALSAR). Furuya et al. (2017) applied the range split-spectrum method (SSM, Gomba et al. 2016) to the two Es episodes in Japan to separate the ionospheric dispersive and tropospheric non-dispersive phases. Successful detections of Es simultaneously by both GNSS TEC and InSAR have still been limited to those two case studies. Moreover, a detailed comparison of GNSS TEC time-series with InSAR data has been lacking and the fine structure of Es remains uncertain.

Here, we report our detection of another daytime Es episode on June 26, 2020, near Shikoku, Japan, using *L*-band ALOS-2/PALSAR-2 InSAR data as well as GNSS TEC from both GEONET and the SoftBank network; following Maeda and Heki (2014, 2015), we did not examine nighttime Es to avoid confusion with the medium-scale traveling ionospheric disturbances (MSTID) that often co-occur. We also use multiple aperture interferometry (MAI) to reveal the spatial gradient of TEC in the along-track (azimuth) direction. Although the along-track gradient of TEC generates apparent shift in azimuth and degrades the coherence necessary for InSAR and SSM, MAI is useful to examine the small-scale TEC distribution. We discuss the spatial and temporal characteristics of the derived quasi-periodic (QP) TEC anomaly, comparing with the nighttime Es observed by MU radar. We also compare the Es migration velocities inferred from the GNSS TEC observations with theoretical Es simulations by Andoh et al. (2020, 2021, 2023).

2 Data and methods

2.1 Multi-GNSS TEC

We used GNSS Receiver Independent Exchange (RINEX) format data from the GEONET and SoftBank network. The GEONET comprises ~ 1300 points of continuous observation and is maintained by the Geospatial Information Authority of Japan (GSI) (Takamatsu et al. 2023). From SoftBank's network, RINEX data are available within the Consortium to utilize the SoftBank original reference sites for Earth and Space Science (CSESS). We resampled the original 1 Hz data into 30-s sampling data to reduce the data amount. The Beidou (BDS) data set is also available in SoftBank's network. We thus used 16 GNSS satellites in total, namely, GPS (G01, G11, and G22), GLONASS (R11 and R12), BDS (C01, C03, C04, C07, and C10), Galileo (E13, E21, and E27), and QZSS (J02, J03, and J07); of these, the C01, C03, C04, and J07 are geostationary satellites and the C07, C10, J02, and J03 are inclined geosynchronous satellites.

The processing strategy to derive the GNSS TEC is the same as described in Maeda and Heki (2014, 2015). After removing a bias from the slant TEC (STEC) data, we convert it to the vertical TEC (VTEC) using the incidence angle of each STEC data and derive the VTEC anomalies as residuals after fitting the VTEC time series with a low-order polynomial function. We assume that the VTEC anomalies originate at 100 km height within a thin layer of ~ 1–2 km (Maeda and Heki 2014) due to the Es and project the ionospheric penetration point (IPP) to the sub-ionospheric point (SIP); VTEC anomalies over the ocean are thus detectable. Despite the multiple GNSS satellites in different azimuths and elevations, the coherent structure in the VTEC anomalies will validate the assumption of 100 km height of IPP within a thin layer and allow us to associate with the Es.

2.2 L-band InSAR and MAI

We use the *L*-band ALOS-2/PALSAR-2 SM1 mode (84 MHz bandwidth, 3 m resolution) data whose center frequency is 1.258 GHz; the incidence angle in the present study is 39.7 degrees. The recurrent period of the ALOS-2 to the same orbit is 14 days and the local time at the descending node is around noon; the flight azimuth direction of descending orbit is 193 degree clockwise from the north. We thus searched for an adequate SAR image that could catch daytime Es events, focusing only on the data acquired in the descending orbit; the ascending orbit passes local nighttime. We also referred to the Rate-of-TEC-Index (ROTI) map derived routinely by the National Institute of Communications and Technology (NICT), based on the GEONET data (https://aer-nc-web.nict.go.jp/GPS/GEONET/RMAP/). The assumption of the 300 km altitude as the IPP in the NICT's ROTI map will generate apparent "double banded"ROTI signatures in the case of Es, which actually originates from ~ 100 km altitude; Maeda and Heki (2014) explain in their Fig. 3 how the wrong assumption in the altitude of TEC anomaly generates "double banded" signature. The primary

SAR image was acquired on June 26, 2020, 03:04 UT (12:04 JST), at which we confirmed an Es episode from the ROTI map; the foEs from the ionosonde at Kokubunji and Yamagawa were 5.0 MHz and 13.1 MHz, respectively. The secondary image was acquired on September 4, 2020, when no Es episode was found in both the ROTI map and ionosonde at Kokubunji and Yamagawa. The InSAR phase indicates relative range changes in radar LOS between the two imaging epochs with respect to the reference area where no anomalies can be assumed (e.g., Hanssen 2001; Simons and Rosen 2015); InSAR data thus do not tell the absolute radar LOS changes at single specified epoch. If the surface displacements between the epochs are negligible, the InSAR phase can measure the changes in the distributions of both TEC and tropospheric water vapor at the two epochs (e.g., Hanssen 2001; Simons and Rosen 2015). Similar to ground surface displacements, InSAR data do not tell the absolute values of TEC and water vapor at single epoch, either. Hence, although the electron density is generally higher in the *F*-layer, the effects from the *F*-layer would be largely canceled unless any localized anomalies in the *F*-layer were present at either primary or secondary (and possibly both) epochs. The localized anomalies from the *E*-layer can be isolated in the daytime images, assuming that the spatial scale of anomalies in the *F*-layer is much greater than that in the *E*-layer.

We combined two continuous ALOS-2/PALSAR-2 images acquired on the path-frame pairs 21-2930 and 21-2940. The imaging areas on the ground and at the height of 100 km are outlined in Fig. 1 with the solid and dotted squares, respectively, and indicate that the spatial scale along the flight (azimuth) direction is the same at both ground level and 100 km height but the scale along the look (range) direction at ionospheric height is extended by a factor of 1.2 at ground level (Meyer et al. 2015; Sato et al. 2021). No shallow earthquakes occurred between the two epochs in the imaged area, meaning that there were no detectable surface displacements. The InSAR processing strategy is the same as our previous reports (Maeda et al. 2016; Furuya et al. 2017), using a commercial software package by gamma remote sensing.

To separate dispersive ionospheric signals from non-dispersive tropospheric signals due to water vapor (e.g., Kinoshita et al. 2013), we use the range SSM, allowing us to perform dual-frequency measurement with the PALSAR-2 data; we set the higher and lower central frequency as 1.284 GHz and 1.231 GHz, respectively, with the bandwidth of 26.5 MHz. Although the bandwidth became one-third of the original one, the interferometric coherence was overall good enough to perform phase unwrapping (Figure S3) robustly and to decompose into dispersive ionospheric and non-dispersive phases using

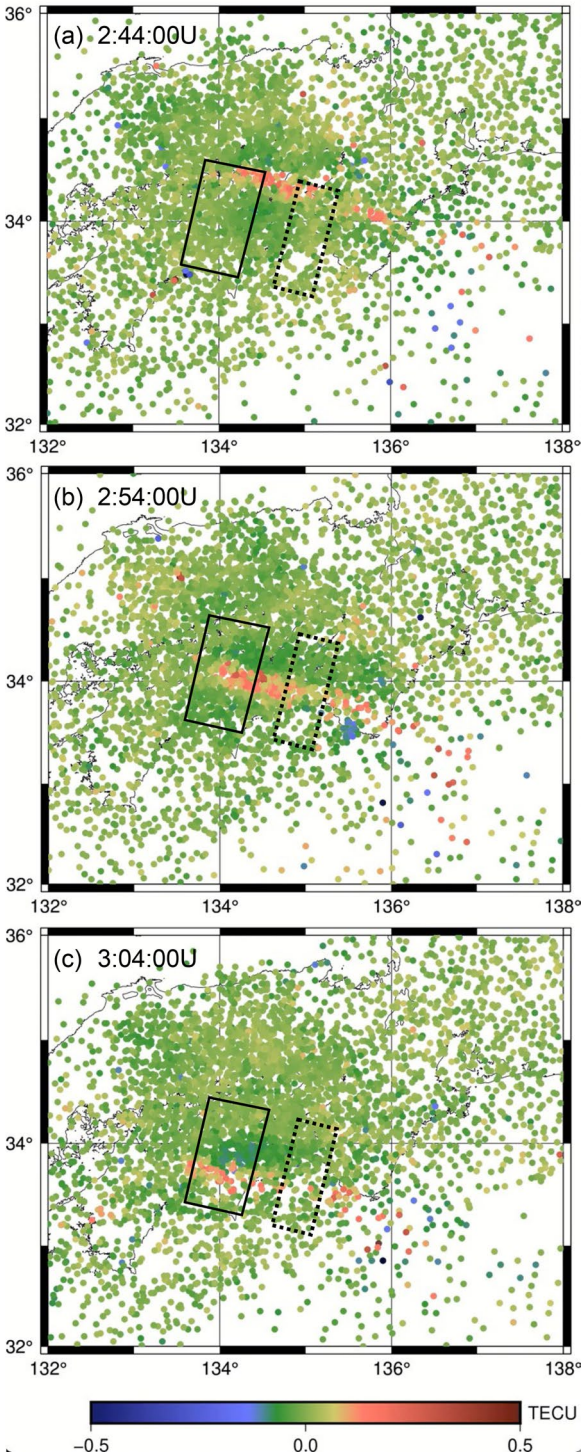

Fig. 1 Three snapshots of the VTEC at **a** 2:44UT, **b** 2:54UT, and **c** 3:04 UT on June 26, 2020. The PALSAR-2 image on the ground outlined with black square was acquired on the same instant as Fig. 1c; the dotted square is the imaged area at the height of 100 km. See Figure S1 to confirm the impact of multi-GNSS and SoftBank's network upon the dense spatial coverage. Also, see Figure S2, a one-hour movie from 2:30 UT

the standard formulation (Gomba et al. 2016; Furuya et al. 2017); coherence is defined as the normalized cross-correlation of the primary and secondary SAR images, taking from the lowest value 0 to the highest value 1, and needs to be high for successful phase unwrapping and SSM. Coherence can be degraded not only from changes in reflectivity but also errors in image matching, the latter of which is the case where the along-track TEC gradient is high. However, we can utilize the high along-track TEC gradient in the MAI-based TEC mapping explained below. We did not remove any long-wavelength phase trends by fitting with a polynomial plane, either, because they would appear in both dispersive and non-dispersive phases.

In addition to InSAR, we perform MAI to extract the changes in along-track TEC gradient (Meyer et al. 2006; Jung et al. 2013; Chen and Zebker 2014) to independently derive the ionospheric signals without relying on the SSM. The MAI technique splits the entire synthetic aperture time into forward- and backward-looking time and forms forward- and backward-looking InSAR images. Taking the difference between them, the MAI originally allows us to derive the large (> ~ 1 m) along-track (near north–south) ground displacements (Bechor and Zebker 2006), whose detection had been difficult because of lower sensitivity than to the up-down and east–west displacements; see Eq. (1) for the relation between the MAI phase data ϕ^{MAI} and along-track (azimuth) displacement δx (Jung et al. 2013). In the absence of real surface displacements, the MAI is useful for detecting spatially heterogeneous ionospheric effect because the gradient of TEC along the azimuth causes the apparent azimuth displacements (or shifts) particularly in the low-frequency SAR data (Meyer et al. 2006; Jung et al. 2013; Chen and Zebker 2014),

$$\phi^{\mathrm{MAI}} = -\frac{2\pi}{l}\delta x = \frac{2\pi}{l\alpha}\frac{40.3}{f^2}\frac{\partial(\Delta \mathrm{TEC})}{\partial x} \tag{1}$$

where l, x and f indicate the antenna length (m), along-track (azimuth) coordinate (m), and carrier frequency (Hz), respectively. The ΔTEC in Eq. (1) is the changes of TEC between the primary and secondary dates. While the "system- and geometry-dependent" factor α (Meyer et al. 2006) was numerically estimated in Jung et al. (2013), Yamashita et al. (2022) derived its analytical expression on the basis of a thin-layer ionosphere model in Kim (2013) as

$$\alpha = \frac{1}{R_0}\frac{v_{\mathrm{sat}}}{v_{\mathrm{piercing}}} = \frac{1}{R_0}\frac{h_{\mathrm{sat}}}{h_{\mathrm{ion}}} \tag{2}$$

where R_0, v_{sat}, and v_{piercing} are the zero Doppler range (approximately equal to the closest range), the satellite velocity, and the velocity of the ionospheric piercing point of LOS, respectively. When no ionospheric motion can be assumed during the azimuth integration time (Kim 2013), the ratio of the velocities is the same as that of the satellite altitude h_{sat} and the effective altitude of the ionosphere h_{ion} as in Eq. (2). Here, the h_{sat} is 630 km, and we may assume that h_{ion} is 100 km because the ionospheric signals are due to the Es. In the present case, we should also take the significant migration velocity of TEC anomaly into account. We set α as 5.9 times the inverse of R_0 because the TEC migration velocity of ~ 90 m/s estimated from GNSS TEC was added to the v_{piercing} of 1.2 km/s and nearly in parallel to the satellite velocity of 7.6 km/s.

Although we can extract the TEC anomaly distribution by integrating the apparent along-track displacements (azimuth shifts) without using the SSM, there is one practical issue. Because the initial values are uncertain for the integration, there arise unrealistic jumps along the range direction if we integrate with the same initial values. Those jumps, however, do not significantly vary along the azimuth and thus can be estimated by averaging them at several locations in the azimuth direction.

To understand the origin of non-dispersive signals, we also examined the radar echo intensity data by Japan Meteorological Agency (JMA), whose weather radar observation network delivers every 10 min over Japan with a spatial resolution of ~ 1 km (http://database.rish.kyoto-u.ac.jp/arch/jmadata/data/jma-radar/synthetic/original/).

3 Results

3.1 Spatial and temporal changes in multi-GNSS VTEC

Figure 1 shows a series of snapshots of the VTEC from 2:44 UT to 3:04 UT every 10 min on June 26, 2020 by GEONET plus Softbank multi-GNSS. The PALSAR-2 image was acquired on 3:04 UT that was the same instant of Fig. 1c; Figure S1 shows the impact of multi-GNSS and SoftBank's network upon the dense spatial coverage, making the average distance between each IPPs from ~ 10 km (Fig S1a) to ~ 5 km (Fig S1b), and ~ 1 km (Fig S1c), and Figure S2 is a 1-h movie from 2:30 UT. Considering the VTEC anomalies by ~ 0.15 TECU as significant, the east–west (EW) elongated pattern is extended over ~ 180 km with the north–south (NS) width of 10–20 km, which are consistent with the previous studies (Maeda and Heki 2014, 2015).

Figure 2a, c shows the time-series data of the VTEC at the IPPs of GEONET sites from QZSS J07 (Fig. 2a) and those at SoftBank sites from BDS C04 (Fig. 2c), respectively; both the QZSS J07 and the BDS C04 are geostationary satellites at 127°E and 160°E, respectively, which are helpful to isolate the migration of TEC anomaly

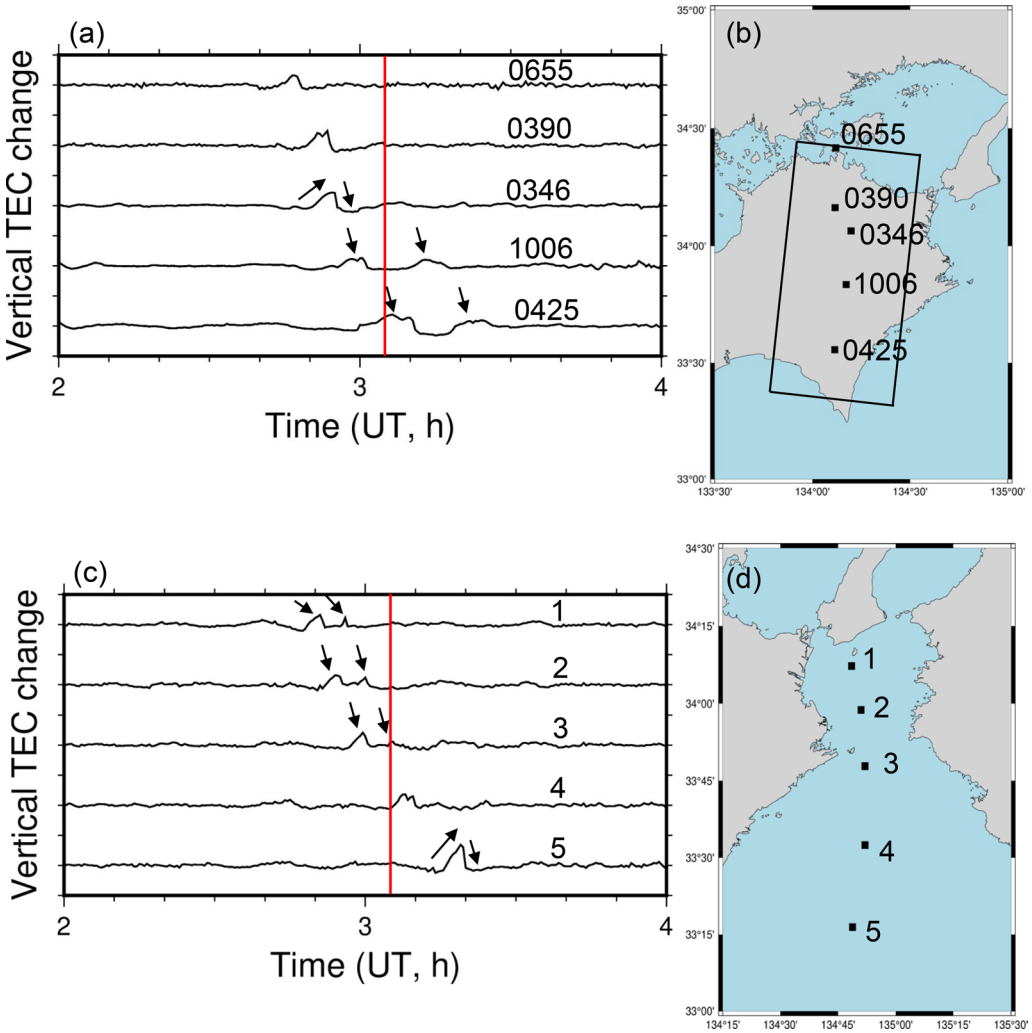

Fig. 2 **a** VTEC time-series data at GEONET sites from QZSS J07, geostationary satellite; the numbers, 0655, 0390, 0346, 1006, and 0425, indicate the site number in GEONET. One vertical tick indicates 0.5 TECU. The red vertical line indicates the instance of PALSAR-2 imaging. The earlier portion in time indicates the frontal side of the VTEC anomaly. **b** Locations of IPPs projected on the ground for each GEONET site. **c** VTEC time-series data at SoftBank sites from BDS C04, geostationary satellite; the numbers, 1, 2, 3, 4, 5, indicate the site number in Softbank network. The horizontal and vertical scales and the red line have the same meanings as in (**a**). **d** Locations of IPPs projected on the ground for each Softbank network site

because the microwave is transmitted from the same location in space. The maximum peak amplitude of the Es signal is 0.22 TECU (1 TECU = 10^{16} electrons/m^2) at the GEONET 0346 (Fig. 2b) and 0.35 TECU at the Softbank 5 (Fig. 2d). Judging from the migration distance of ~ 100 km during the 20 min in Figs. 1 and 2a, c, we infer that the migration speed of the VTEC anomaly is ~ 90 m/s to the south; the southward migration is also evident from the movie (Figure S2). Figure 2a, c indicates that the leading VTEC anomaly gradually increases from the frontal side of the propagation direction and abruptly decreases toward the lee side at rates of ~ 0.04 TECU/min and ~ 0.2 TECU/min, respectively; we annotated with arrows for the site 0346 in Fig. 2a and the site 5 in Fig. 2c. Moreover, at the GEONET 1006 and 0425 annotated with arrows (Fig. 2a), we can spot a secondary peak in the VTEC time-series that also propagates toward the south direction. There are similar but smaller secondary peak at the SoftBank 1, 2 and 3 (Fig. 2c) annotated again with arrows.

The SAR imaging is essentially done at the instant of the red line in Fig. 2a, c. Although the first VTEC peak at the IPP of 0425 in Fig. 2a matches the instant, the IPP is projected ~ 80 km to the west and outside the SAR image on the ground. No other first leading VTEC peaks in Fig. 2a, c match the instant of SAR imaging, and thus unfortunately we cannot associate the first peaks in the presented VTEC time-series with the anomalies in SAR

image; this is also evident in the sparse IPPs inside the dotted square in Fig. 1c. However, we discuss below the possible correspondence of the peaks in the VTEC time-series to the anomalies in SAR images.

3.2 Ionospheric and non-ionospheric signals from InSAR

Figure 3a, b shows the ionospheric (dispersive) and non-ionospheric (non-dispersive) phases derived from the SSM; Fig. 3 shows the results right after the SSM, where we have not applied any additional smoothing filter. Comparing Fig. 3a, b with the original full-bandwidth InSAR data (Figure S3a), we observe that the ionospheric (Fig. 3a) and non-ionospheric (Fig. 3b) signals are distinctly separated with exceptions of the "sandy storm" E–W elongated striation around the middle and those indicated with black arrows in Fig. 3a, b. Those exceptions are attributable to the lower coherence (Figure S3b). As there are no east–west trending structures on the ground surface, the low-coherence streak around the middle of Fig S3b is presumably due to the azimuth shift δx in Eq. (1) by the along-track gradient of TEC and resulting matching errors.

In the ionospheric signals (Fig. 3a), we observe at least two EW-trending phase anomalies, one smaller to the north and another larger one to the south indicated with two white arrows to the west; another EW-trending phase anomaly is buried in the low coherence area but marginally observed, indicated with white arrow to the east. To compare with the GNSS TEC, we converted the phase data in Fig. 3a into the VTEC anomaly in Fig. 3c. We simply mapped (slant) TEC into VTEC, considering the incidence angle. We also show the VTEC anomaly profile in Fig. 3d along the black line in Fig. 3c. The VTEC anomaly to the south shows a gradual increase from the frontal side of the propagation direction and an abrupt decrease toward the lee side at rates of ~ 0.022 TECU/km and ~ 0.13 TECU/km, respectively (Fig. 3d). Using the increasing rate of ~ 0.04 TECU/minutes in Fig. 2, we can estimate the migration velocity of 109 m/s, which is largely consistent with the estimated velocity from Figs. 1 and 2. Thus, although none of the GNSS receivers in Fig. 2 detected the first leading TEC anomaly at the instant of SAR imaging as noted before, the larger EW-trending anomaly to the south in Fig. 3a, c presumably corresponds to the leading VTEC anomaly in the time series of Fig. 2a, c. The smaller EW-striation to the north in Figs. 3a and 3c is separated by 15–20 km from the larger southern one, and its VTEC amplitude is less than half of that. Assuming the same migration velocity of ~ 90 m/s, the temporal separation would be ~ 3–4 min. The second major EW-striation to the north in Fig. 3a, c thus corresponds to the secondary peaks at SoftBank 2 and 3 in Fig. 2c, and the one at Softbank 3 seems to match the instant of SAR imaging. While the second largest blob at 1006 and 0425 in Fig. 2a are outside the SAR image, it is separated from the first blob by ~ 50 km, and the width seems to be much broader in view of Figure S2.

In contrast to the multiple LOS directions in Fig. 1, the InSAR phase is derived only from a single LOS direction. Nonetheless, the inferred gradual increase in the frontal side and abrupt steepening in the backside in Fig. 2a, c and 3d are consistent, supporting our assumption of a thin Es layer. It should be noted that Fig. 3a, c could also include the effect of the *F*-layer, which may be responsible for the long-wavelength signals in Fig. 3a, c as well as the negative amplitude in Fig. 3c.

The non-ionospheric signals in Fig. 3b indicate long-wavelength phase changes and small-scale phase anomalies around the northwest corner; no similar phases are found in Fig. 3a. We confirmed that the weather radar echo indicated local precipitation of ~ 20 mm/hour on September 4, 2020 but no such anomalies on June 26, 2020 (Figure S4). The small-scale phase anomalies are thus presumably due to the tropospheric water vapor signals associated with a heavy rain event on September 4, 2020 (e.g., Kinoshita et al. 2013).

3.3 MAI data

Figure 4a is the azimuth shift δx derived from the unwrapped MAI phase. Given the absence of real surface displacements during the imaging period, Fig. 4a indicates the spatial pattern of the TEC gradient along the flight direction; see Eq. (1). We can estimate the distribution of TEC by integrating the shift data in Fig. 4a along the flight direction (Jung et al. 2013; Chen and Zebker 2014; Yamashita et al. 2022). We can associate the multiple EW-trending anomalies indicated with black and white arrows in Fig. 4b with the negative and positive pairs in Fig. 4a. The negative and positive shifts in Fig. 4a correspond to the increasing and decreasing trend of TEC along the azimuth direction, respectively; see Eq. (1). When the magnitude and the spatial extent of both negative and positive shift are comparable along the azimuth direction, the TEC distribution will be symmetric across a local peak of TEC in the azimuth direction. At the significant negative and positive pairs to the south in Fig. 4a indicated with ovals, the magnitude of the negative shift is greater than that of the positive shift, and the spatial extent of the positive shift along the azimuth is broader than that of the negative shift. Thus, when viewed from the inverse direction to the flight (azimuth) direction, Fig. 4b indicates the gradual increase of TEC from the frontal side and abrupt decrease of TEC in the lee side, which is consistent with Figs. 2 and 3. The MAI-based VTEC in Fig. 4b is less noisy than the SSM-based VTEC in Fig. 3c, the latter of which is more

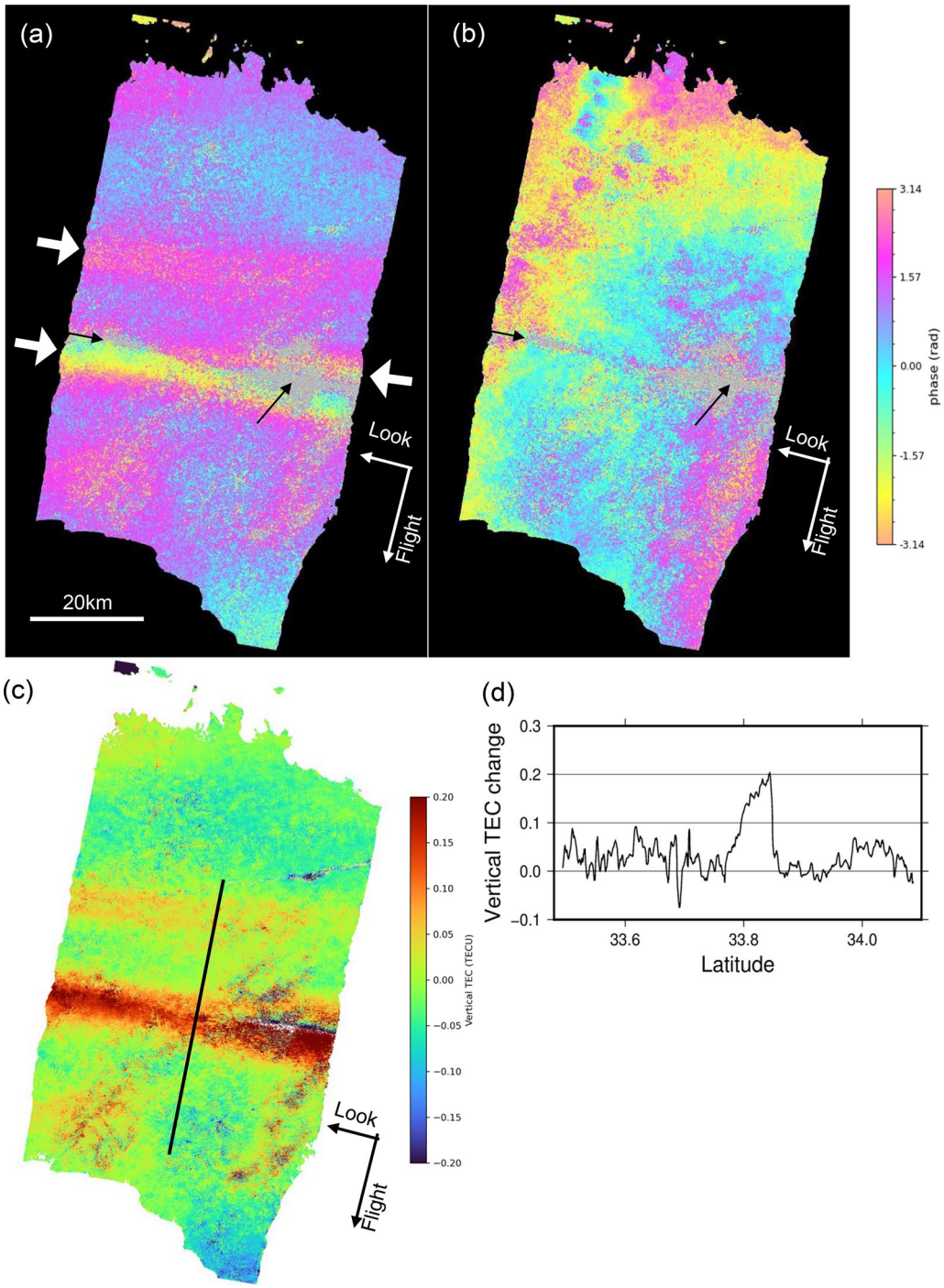

Fig. 3 Results of SSM. **a** Dispersive ionospheric phase indicated with three white arrows, **b** Non-dispersive tropospheric delay phase. "Sandy storm" phases near the middle eastern area with black arrows would be caused by lower coherence; see Fig. S3b. No shallow earthquakes occurred during the period. Although we cannot specify the date and time of each phase only from InSAR data, we can interpret from ionosonde, GNSS TEC, and weather radar data that the ionospheric phase in (**a**) and the tropospheric phase in (**b**) originate from June 26, 2020 and September 4, 2020, respectively; see the texts for details. (**c**) VTEC anomaly map derived from Fig. 3a. The white pixels around the major TEC striation indicate missing data; see the coherence map (Fig S3b). (**d**) The VTEC profile along the black line in Fig. 3c

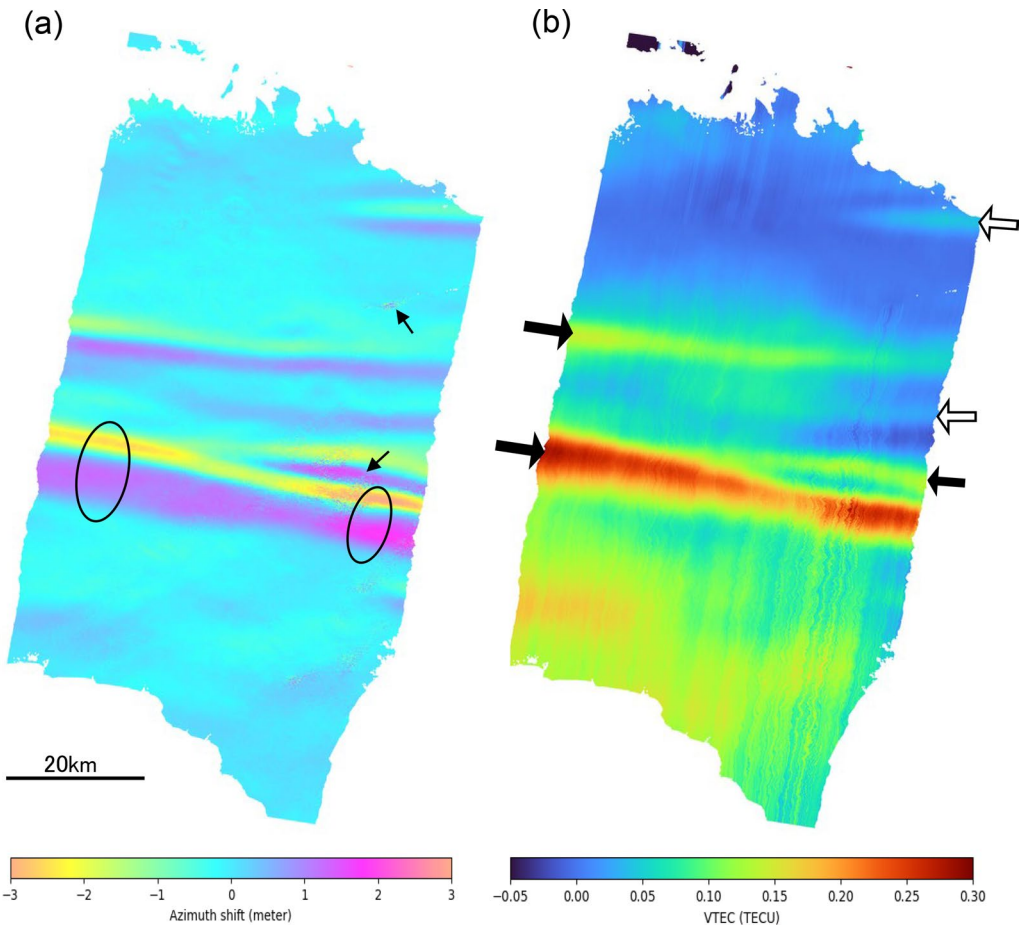

Fig. 4 **a** Apparent azimuth displacements in meter derived from the unwrapped MAI phase, indicating the distribution of along-track TEC gradient; see Eq. (1). Solid ovals indicate the typical TEC gradient zones for backside steepening of TEC. Two black arrows indicate low coherence areas. **b** VTEC distribution is derived by integrating the TEC gradient along the along-track (azimuth) axis and mapping into the vertical direction. We also need to consider the effective ionosphere piercing velocity; see Eqs. (1) and (2) and the main text. Note the similar but more complete distribution of TEC than Fig. 3c

strongly affected by the coherence (Figure S3b) and less sensitive to changes in the NS direction. Figure 4b thus reveals even minor TEC anomalies with amplitude ~ 0.05 TECU or below as indicated with white arrows, suggesting that we may associate much smaller peaks in GNSS TEC time series with Es-related signals. The coherence loss due to the large azimuth shift becomes insignificant in MAI because of the cancellation between the forward- and backward-looking InSAR data. However, the many NS-trending wavy lines around the east in Fig. 4b are artifacts due to the residual low coherence phases in Fig. 4a indicated with thin black arrows.

4 Discussion

4.1 Es migration velocities in numerical simulation and TEC observations

Based on the wind shear theory of Es generation, Andoh et al. (2020, 2021, and 2023) performed 3D numerical simulations of Es layers to examine their spatial and temporal evolution and their relations to neutral winds driven by atmospheric tides; the 3D neutral winds were derived from the GAIA (Ground-to-topside model of Atmosphere and Ionosphere for Aeronomy) model (Jin et al. 2011). Their simulated migration velocities of Es are on the order of 0.1–1.0 m/s and turn out to be an order-of-magnitude or much slower than our inferred velocities in Figs. 2 and 3, which were southward migration with ~ 90 m/s around the local noon; the migration velocities of TEC anomaly reported in Maeda and Heki (2015) were of similar magnitude.

As a possible cause for the apparent discrepancy, Andoh et al. (2023) suggested the large differences in the spatial resolution of their simulating neutral wind and an influence of atmospheric gravity wave. While the much finer spatial resolution may help resolve the discrepancy, we interpret that the migration (propagation) velocities

in Andoh et al.'s simulations are physically different from what the GNSS TEC and the InSAR ionospheric phase have revealed. Because we also consider the wind shear as the primary generation mechanism of a thin metallic ion layer, the horizontal velocities of the Es-generation (metallic ion) layer would be those of the neutral winds averaged around just above and below the Es-generation altitude, which would be what Andoh et al. (2023) have demonstrated. The velocities of the metallic ion layer will then be inevitably close to null and slower than the velocities of neutral winds. On the other hand, no Es layers will grow thicker over time, probably because both the top and bottom sides of the Es layer generated by zonal wind shear are known to be unstable due to the wind-driven gradient drift mechanism (Kagan and Kelly 1998). Thus, we speculate that any newly formed Es (metallic ion) layers will be torn off and drift away. The horizontal migration of TEC anomaly would be the advection of such dispatched Es possibly by neutral winds, because the observed Es migration velocities are on the same order as the simulated meridional wind velocities (Andoh et al. 2023). The detailed mechanisms, however, remain uncertain. The fine spatial TEC distribution during Es previously inferred from GNSS TEC time-series data (Maeda and Heki 2015; Saito et al. 2021) could be confirmed as a spatial snapshot by InSAR and MAI, meaning that what GNSS TEC and L-band SAR detected in the ionosphere are genuine and could become a future target of simulation studies.

4.2 Quasi-periodic TEC signatures in daytime Es

Maeda and Heki (2015) pointed out quasi-periodic (QP) TEC signatures from the time series of GNSS TEC data; the QP signatures were unclear from the VTEC map due to the lower spatial resolution. In the present study, the secondary peak in the VTEC time series (Fig. 2) and the multiple EW-trending TEC anomalies of ~ 5–10 km width with ~ 10–20 km spacing in InSAR and MAI data (Figs. 3a, c and 4) verify the presence of such structures. In particular, the multiple positive and negative pairs in the azimuth shift by MAI evidently demonstrate the fine spatial distribution of TEC during the Es episode (Fig. 4). The QP TEC signatures in this study belong to the type oriented across-the-elongation direction, and the Es episode on May 25, 2016, reported by Furuya et al. (2017), also showed the across-the-elongation structure. On the other hand, the Es episodes on July 11, 2011 reported by Maeda and Heki (2015) and on June 28, 2009, reported by Maeda et al. (2016) and Furuya et al. (2017), shows the QP TEC structure along the elongation direction; Maeda (2015) also pointed out other episodes with the similar structure. It is important to note that both types appear quasi-periodically and are largely the same in terms of the spatial scales of width and separation of each TEC anomaly. As discussed below, we speculate that the distribution of neutral winds causing the Kelvin–Helmholtz (KH) instability (Larsen 2000) determines which type appears.

We should comment on the differences between the QP TEC signatures and the "QP echoes" detected by MU radar (Yamamoto et al. 1991). The QP echoes by MU radar are observed only during nighttime Es and no similar echoes were known in daytime Es (Yamamoto et al. 1991); Thampi et al. (2010) exceptionally detected the QP echoes from daytime Es by MU radar during a partial solar eclipse. Another essential structure of the QP echoes is that they are vertically extended by as much as 30 km and aligned along the local geomagnetic field lines (e.g., Maruyama et al. 2000; Ogawa et al. 2002; Saito et al. 2006). We cannot estimate the thickness of the Es from either GNSS or InSAR because both of the TEC data are the "integrated" electron content along the radar LOS. No nearby ionosonde does not allow us to estimate the thickness as in Maeda and Heki (2014), either. However, despite their different LOS directions, the spatial distributions of VTEC from both GNSS, InSAR and MAI are generally consistent, supporting our assumption of thin Es layer. Moreover, we note that the periodicity itself is not as clear as that of nighttime QP echoes because the peak TEC amplitude behind the leading striation is significantly smaller and variable, and the NS width, EW length and separation of each striation are also variable. These characteristics are, however, consistent with what were pointed out in Maeda and Heki (2015) and Maeda (2015).

Why are there no significant vertical structures in daytime Es? To account for both the QP echoes in the nighttime Es and the QP scintillation in the satellite VHF radio signal, Maruyama et al. (2000) proposed a model that forms a current closure sheet from a large polarization electric field at the height of the Es layer to the upper normal *E* layer; their assumed EW-elongated plasma cloud is the same as our observations have indicated in terms of the orientation (Figs. 3 and 4). Based on this model, we may attribute the lack of vertically extended structure in daytime Es to the daytime higher production rate of ions and electrons, significantly reducing the plasma density gradient and making the integrated Pedersen conductivities in the upper *E* region much higher than those in nighttime. Consequently, as Yokoyama et al. (2004) simulated, the polarization electric field at higher altitudes is shorted out and no field-aligned structure will be developed.

Our observations show that daytime Es is accompanied by multiple horizontal striations that appear quasi-periodically. The wind shear in the Es layer can readily

generate KH instability and subsequent eddies of the neutral atmosphere will reveal periodic structure (Larsen 2000; Bernhardt 2002). Although the KH instability was initially proposed to account for the QP echoes by MU radar, and Maeda et al. (2016) discussed its role for the generation of spatial structure, the backside steepening of Es plasma blob confirmed in this study is also reminiscent of the fluctus clouds associated with KH instability.

4.3 Backside steepening of Es plasma blob

Based on the quasi-periodic scintillation observations of the 136-MHz transmission from a geostationary satellite, Maruyama (1991) suggested an Es plasma blob in the night whose density gradually increases from the frontal leading edge but steeply drops in the backside; see Fig. 6 in Maruyama (1991). Maeda and Heki (2015) and Saito et al. (2021) also suggested such a shape from the daytime GNSS TEC time-series data, and Fig. 2a, c is consistent with these observations. Notably, the InSAR and MAI data in Figs. 3 and 4 are independent confirmations of such asymmetric distributions of TEC in the spatial dimension. However, at first glance, the backside steepening is counter-intuitive because, when any frontal structure passes by over undisturbed area, we will expect an abrupt rise at the frontside but a long-lasting tail in the backside for the initiated disturbance to be calmed down; if one takes an analogy of southward migrating meteor or comet, we will expect a longer tail in the northward. Although Maruyama (1991) suggested the gradient drift instability mechanism by polarization electric field, it is uncertain if and how such a polarization electric field could be maintained during daytime Es as argued by Saito et al. (2021). We consider that the backside steepening of the plasma blob includes important but unclarified physics of Es. Further new observations and theoretical studies are necessary but deferred for future research.

5 Summary

Using the nationwide GNSS networks and the satellite *L*-band SAR data, we have revealed the fine structure of a mid-latitude daytime Es episode in Japan. The MAI technique was applied to an Es for the first time and helped clarify the detailed TEC distribution without being seriously affected by the low coherence problem of SSM. The MAI-based VTEC map revealed multiple EW-trending TEC striations, some of which were impossible to identify in both GNSS VTEC and InSAR SSM data. The peak VTEC changes in each striation range from ~ 0.05 TECU in the shorter and narrower striation to 0.25 TECU in the leading longest striation. Although the precise length in EW direction of each striation is uncertain in SAR images, the width of each striation ranges from ~ 5 km for the small and shorter one to ~ 10–15 km for the large and longer one. Each striation is separated in NS direction by 5–20 km. As previously suggested in GNSS TEC time series, we confirmed the asymmetric electron density distribution in the leading primary EW-elongated TEC striation that gradually increases from the frontal leading edge but abruptly drops in the trailing edge, which requires further understanding of the mechanisms.

Abbreviations

ALOS-2	Advanced Land Observing Satellite-2
CSESS	Consortium to utilize the SoftBank original reference sites for Earth and Space Science
Es	Sporadic-E layer
GAIA	Ground-to-topside model of Atmosphere and Ionosphere for Aeronomy
GEONET	GNSS Earth Observation Network
GNSS	Global Navigation Satellite System
GSI	Geospatial Information Authority of Japan
InSAR	Interferometric Synthetic Aperture Radar
IPP	Ionospheric penetration point
KH	Kelvin–Helmholtz
LOS	Line of sight
MAI	Multiple aperture interferometry
MSTID	Medium-scale traveling ionospheric disturbances
MU	Middle and upper atmosphere
NICT	National Institute of Communications and Technology
PALSAR-2	Phased Array-type L-band Synthetic Aperture Radar-2
QP	Quasi-periodic
RINEX	Receiver independent exchange
ROTI	Rate-of-TEC-Index
SAR	Synthetic aperture radar
SIP	Sub-ionospheric penetration point
SM1	Stripmap 1
SSM	Split spectrum method
STEC	Slant total electron content
TEC	Total electron content
VHF	Very high frequency
VTEC	Vertical total electron content

Supplementary Information

The online version contains supplementary material available at https://doi.org/10.1186/s40623-024-02086-5.

Additional file 1.

Additional file 2.

Acknowledgements

We thank Jun Maeda for the discussion on the earlier results. We also thank two anonymous reviewers for their careful and detailed comments that were helpful to improve the clarity of the original manuscript.

Author contributions

TF performed all the data processing. MF and KH conceptualized and supervised, and MF drafted the manuscript.

Funding

The work is funded by the Hokkaido University.

Availability of data and materials

The GNSS observation data from GEONET can be accessed at the Geospatial Information Authority of Japan (GSI); we used the 30-s sampling RINEX data available from GSI (http://terras.gsi.go.jp). The SoftBank's GNSS observation data in this study was provided by SoftBank Corp. and ALES Corp. through the framework of the CSESS. ROTI data based on GEONET GNSS data are available from NICT (https://aer-nc-web.nict.go.jp/GPS/GEONET/RMAP/). JMA's weather radar data are available from Kyoto University (http://database.rish.kyoto-u.ac.

jp/arch/jmadata/data/jma-radar/synthetic/original/). The ALOS-2/PALSAR-2 level 1.1 data are shared among PIXEL (PALSAR Interferometry Consortium to Study our Evolving Land surface) and provided by JAXA under a cooperative research contract with PIXEL. The ownership of PALSAR-2 data belongs to JAXA. This study was supported by ERI JURP 2021-B-03 in Earthquake Research Institute, the University of Tokyo. The ALOS-2/PALSAR-2 level 1.1 data can also be searched and purchased from either PASCO (http://en.alos-pasco.com) or RESTEC (https://www.restec.or.jp/en/), which are the authorized data providers from JAXA. ALOS-2/PALSAR-2 level 1.1 data are also available if your research proposal for Earth observation using satellite images is accepted through reviewing processes, although the announcement is launched irregularly (https://www.eorc.jaxa.jp/ALOS/en/index_e.htm).

Declarations

Ethics approval and consent to participate
Not applicable.

Competing interests
The authors declare that they have no competing interests.

Author details
[1]Department of Natural History Sciences, Graduate School of Science, Hokkaido University, Sapporo, Japan. [2]Department of Earth and Planetary Sciences, Faculty of Science, Hokkaido University, Sapporo, Japan. [3]Department of Earth and Planetary Sciences, Faculty of Science, Hokkaido University, Shanghai Astronomical Observatory, Shanghai, China.

Received: 21 March 2024 Accepted: 16 October 2024
Published online: 30 October 2024

References

Andoh S, Saito A, Shinagawa H, Ejiri MK (2020) First simulations of day-to-day variability of mid-latitude sporadic E layer structures. Earth Planet Space 72:165. https://doi.org/10.1186/s40623-020-01299-8

Andoh S, Saito A, Shinagawa H (2021) Temporal evolution of three-dimensional structures of metal ion layer around Japan simulated by a mid-latitude ionospheric model. J Geophys Res Space Phys 126:e2021JA029267. https://doi.org/10.1029/2021JA029267

Andoh S, Saito A, Shinagawa H (2023) Simulation of horizontal sporadic E layer movement driven by atmospheric tides. Earth Planets Space 75:86. https://doi.org/10.1186/s40623-023-01837-0

Bechor NBD, Zebker HA (2006) Measuring two-dimensional movements using a single InSAR pair. Geophys Res Lett 33:L16311. https://doi.org/10.1029/2006GL026883

Bernhardt PA (2002) The modulation of sporadic-E layers by Kelvin-Helmholtz billows in the neutral atmosphere. J Atmos Solar-Terrestrial Phys 64(12–14):1487–1504. https://doi.org/10.1016/S1364-6826(02)00086-X

Chen AC, Zebker HA (2014) Reducing ionospheric effects in InSAR data using accurate coregistration. IEEE Trans Geosci Remote Sens 52(1):60–70. https://doi.org/10.1109/TGRS.2012.2236098

Furuya M, Suzuki T, Maeda J, Heki K (2017) Midlatitude sporadic-E episodes viewed by L-band split-spectrum InSAR. Earth Planets Space 69:175. https://doi.org/10.1186/s40623-017-0764-6

Gomba G, Parizzi A, De Zan F, Eineder M, Bamler R (2016) Toward operational compensation of ionospheric effects in SAR interferograms: the split-spectrum method. IEEE Trans Geosci Remote Sens 54(3):1446–1461. https://doi.org/10.1109/TGRS.2015.2481079

Haldoupis C (2011) A tutorial review on sporadic E layers. In: Abdu MA, Pancheva D (eds). Aeronomy of the earth's atmosphere and ionosphere. Springer, Netherlands, pp 381–394. https://doi.org/10.1007/978-94-007-0326-1_29

Hanssen RF (2001) Radar Interferometry: Data Interpretation and Error Analysis. Kluwer Academic Publishing

Jin H, Miyoshi Y, Fujiwara H, Shinagawa H, Terada K, Terada N, Ishii M, Otsuka Y, Saito A (2011) Vertical connection from the tropospheric activities to the ionospheric longitudinal structure simulated by a new Earth's whole atmosphere-ionosphere coupled model. J Geophys Res Space Phys 116:A01316. https://doi.org/10.1029/2010JA015925

Jung H-S, Lee D-T, Lu Z, Won J-S (2013) Ionospheric correction of SAR interferograms by multiple-aperture interferometry. IEEE Trans Geosci Remote Sens 51(5):3191–3199. https://doi.org/10.1109/TGRS.2012.2218660

Kagan LM, Kelley MC (1998) A wind-driven gradient drift mechanism for mid-latitude E-region ionospheric irregularities. Geophys Res Lett 25:4141–4144. https://doi.org/10.1029/1998GL900123

Kim JS (2013) Development of ionosphere estimation techniques for the correction of SAR data, Dissertation, ETH Zurich.

Kinoshita Y, Shimada M, Furuya M (2013) InSAR observation and numerical modeling of the water vapor signal during a heavy rain: a case study of the 2008 Seino event, central Japan. Geophys Res Lett 40:4740–4744. https://doi.org/10.1002/grl.50891

Larsen MF (2000) A shear instability seeding mechanism for quasi-periodic radar echoes. J Geophys Res 105(A11):24931–24940. https://doi.org/10.1029/1999JA000290

Maeda J, Heki K (2014) Two-dimensional observations of midlatitude sporadic E irregularities with a dense GPS array in Japan. Radio Sci 49:28–35. https://doi.org/10.1002/2013RS005295

Maeda, J. (2015a) Morphology and dynamics of midlatitude sporadic-E from GPS total electron content observations. Dissertation, Hokkaido University

Maeda J, Heki K (2015b) Morphology and dynamics of daytime mid-latitude sporadic-E patches revealed by GPS total electron content observations in Japan. Earth Planet Space 67:89. https://doi.org/10.1186/s40623-015-0257-4

Maeda J, Suzuki T, Furuya M, Heki K (2016) Imaging the midlatitude sporadic E plasma patches with a coordinated observation of spaceborne InSAR and GPS total electron content. Geophys Res Lett 43:1419–1425. https://doi.org/10.1002/2015GL067585

Maruyama T (1991) Observations of quasi-periodic scintillations and their possible relation to the dynamics of Es plasma blobs. Radio Sci 26(3):691–700. https://doi.org/10.1029/91RS00357

Maruyama T, Fukao S, Yamamoto M (2000) A possible mechanism for echo striation generation of radar backscatter from midlatitude sporadic E. Radio Sci 35(5):1155–1164. https://doi.org/10.1029/1999RS002296

Mathews JD (1998) Sporadic E: current views and recent progress. J Atmos Terr Phys 60(4):413–435

Meyer F, Bamler R, Jakowski N, Fritz T (2006) The potential of low-frequency SAR system for mapping ionospheric TEC distributions. IEEE Geosci Remote Sens Lett 3(4):560–564. https://doi.org/10.1109/LGRS.2006.882148

Meyer F, Chotoo K, Chotoo SD, Huxtable BD, Carrano CS (2015) The influence of equatorial scintillation on L-Band SAR image quality and phase. IEEE Geosci Remote Sens 54(2):869–880. https://doi.org/10.1109/TGRS.2015.2468573

Muafiry I, Heki K, Maeda J (2018) 3D tomography of midlatitude sporadic-E in Japan from GNSS-TEC data. Earth Planets Space 70:45. https://doi.org/10.1186/s40623-018-0815-7

Ogawa T, Takahashi O, Otsuka Y, Nozaki K, Yamamoto M, Kita K (2002) Simultaneous middle and upper atmosphere radar and ionospheric sounder observations of midlatitude E region irregularities and sporadic E layer. J Geophys Res 107(A10):1275. https://doi.org/10.1029/2001JA900176

Ohta Y, Ohzono M (2022) Potential for crustal deformation monitoring using a dense cell phone carrier global navigation satellite system network. Earth Planets Space 74:25. https://doi.org/10.1186/s40623-022-01585-7

Saito S, Yamamoto M, Hashiguchi H, Maegawa A (2006) Observation of three-dimensional structures of quasi-periodic echoes associated with mid-latitude sporadic-E layers by MU radar ultra-multi-channel system. Geophys Res Lett 33:L14109. https://doi.org/10.1029/2005GL025526

Saito S, Hosokawa K, Sakai J, Tomizawa I (2021) Study of structures of the sporadic E layer by using dense GNSS network observations. Navigation 68:751–758. https://doi.org/10.1002/navi.454

Sato H, Kim JS, Otsuka Y, Wrasse CM, Rodrigues de Paula E, Rodrigues de Souza J (2021) L-band Synthetic Aperture Radar observation of ionospheric density irregularities at equatorial plasma depletion region. Geophys Res Lett 48:e2021GL093541. https://doi.org/10.1029/2021GL093541

Simons M, Rosen PA (2015) Interferometric Synthetic Aperture Radar Geodesy. In: Schubert G (editor-in-chief) Treatise on Geophysics, 2nd edition, Vol 3. Oxford: Elsevier. pp. 339-385

Sun W, Zhao X, Hu L, Yang S, Xie H, Chang S, Ning B, Li J, Liu L, Li G (2021) Morphological characteristics of thousand-kilometer-scale Es structures over China. J Geophys Res Space Phys 126(2):e2020JA028712. https://doi.org/10.1029/2020JA028712

Takamatsu N, Muramatsu H, Abe S, Hatanaka Y, Furuya T, Kakiage Y, Ohashi K, Kato C, Ohno K, Kawamoto S (2023) New GEONET analysis strategy at GSI: daily coordinates of over 1300 GNSS CORS in Japan throughout the last quarter century. Earth Planets Space 75:49. https://doi.org/10.1186/s40623-023-01787-7

Thampi SV, Yamamoto M, Liu H, Saito S, Otsuka Y, Patra AK (2010) Nighttime-like quasi periodic echoes induced by a partial solar eclipse. Geophys Res Lett 37:L09107. https://doi.org/10.1029/2010GL042855

Whitehead JD (1989) Recent work on mid-latitude and equatorial sporadic-E. J Atmos Terr Phys 51(5):401–424

Yamamoto M, Fukao S, Woodman RF, Ogawa T, Tsuda T, Kato S (1991) Midlatitude E region field-aligned irregularities observed with the MU radar. J Geophys Res 96:15943–15949

Yamashita T, Morishita Y, Kobayashi T (2022) Mitigation of Ionospheric Noise in Azimuth Offset Based on the Split-Spectrum Method. IEEE Trans Geosci Remote Sens 60:1–11. https://doi.org/10.1109/TGRS.2021.3073511

Yokoyama T, Yamamoto M, Fukao S, Cosgrove RB (2004) Three-dimensional simulation on generation of polarization electric field in the midlatitude E-region ionosphere. J Geophys Res 109:A01309. https://doi.org/10.1029/2003JA010238

Publisher's Note